Research Square

Preprints are preliminary reports that have not undergone peer review.
They should not be considered conclusive, used to inform clinical practice,
or referenced by the media as validated information.

Insights into the February 2026 Floods in the Tropical Andes of Southern Peru from Satellites and Models

Steven Paul Chavez

steven.chavez@pucp.edu.pe

Pontificia Universidad Católica del Perú: Pontificia Universidad Catolica del Peru
https://orcid.org/0000-0002-1591-0782

Malarvizhi Arulraj

University of Maryland

Research Article

Keywords:

Posted Date: November 23rd, 2026

DOI: https://doi.org/10.21203/rs.3.rs-10962279/v1

License: This work is licensed under a Creative Commons Attribution 4.0 International License.
Read Full License

Insights into the February 2026 Floods in the Tropical Andes of Southern Peru from Satellites and Models.

Steven P. Chavez[1*] and Malarvizhi Arulraj[2]

[1]Pontificia Universidad Católica del Perú, Lima, Perú. [2]Earth System Science Interdisciplinary Center, University of Maryland, College Park, 20740, Maryland, USA.

*Corresponding author: Steven Chavez (steven.chavez@pucp.edu.pe)

Abstract:

Flash floods triggered by intense rainfall during El Niño Costero events pose a major hazard in the Tropical Andes of southern Peru. In February 2026, two consecutive extreme rainfall events caused catastrophic flooding and debris flows in Arequipa, resulting in loss of life, widespread infrastructure damage, and major disruptions to essential services. This study investigates the meteorological conditions associated with these flood-producing storms and evaluates the performance of near-real-time (NRT) and standard versions of the IMERG, GSMaP, and PERSIANN satellite precipitation products in capturing their spatial and temporal evolution. ERA5 reanalysis indicates that enhanced low-level Pacific moisture transport interacting with the steep western slopes of the Andes created favorable conditions for localized afternoon convection and intense rainfall over the Arequipa region. Rain gauge observations revealed highly localized hourly rainfall exceeding 20 mm h^{-1} during the two flood events. Among the satellite products evaluated, IMERG most accurately reproduced the spatial distribution and total accumulation of precipitation, including the localized rainfall maximum over Arequipa, whereas GSMaP and PERSIANN substantially underestimated rainfall amounts. Although the NRT products generally captured the timing and spatial organization of the rainfall better than their standard counterparts, all products underestimated peak rainfall intensity during the most intense convective periods. These findings demonstrate the value of satellite precipitation products for situational awareness and flood monitoring in mountainous regions with sparse ground observations while highlighting the continuing challenges of accurately representing short-duration, terrain-induced extreme rainfall in operational precipitation estimates.

Keywords:

Flooding, Coastal El Nino, Satellite Precipitation, Tropical Andes

1. Introduction

Peru is highly vulnerable to a range of natural hazards, including earthquakes, flash floods, landslides, and debris flows, which pose significant threats to lives, livelihoods, and the national economy (Young and León, 2009). In particular, the increasing frequency and intensity of extreme precipitation events in recent decades have heightened risks to households and communities across the country (Castellares et al., 2015). Southern Peru is especially susceptible to intense precipitation and its associated hazards, owing in part to the influence of El Niño Costero (Coastal El Niño), which can trigger severe flooding, landslides, and debris flows.

The El Niño–Southern Oscillation (ENSO) strongly influences South American climate through coastal warming, enhanced convection, shifts in the Walker circulation, and Rossby wave trains (Cai et al., 2020). Its impacts are further modulated by intrinsic ENSO diversity (Sulca et al., 2018; Cai et al., 2020). El Niño Costero is a distinct type of El Niño that features rapid, localized sea surface temperature (SST) warming in the far eastern tropical Pacific off Peru and Ecuador. Unlike basin-scale ENSO events, these can develop under neutral or La Niña conditions in the central Pacific and remain confined to the eastern sector (Peng et al., 2019; Martinez-Villalobos et al., 2024). This coastal warming propagates southward, weakening the southeast trade winds and advecting warm, moist air masses to higher latitudes (Peng et al., 2019; Martinez-Villalobos et al., 2024). Adding to the pre-existing warming between 10°S and 30°S, El Niño Costero can further amplify extreme rainfall through northerly wind anomalies that intensify moisture transport toward southern Peru (Arequipa, Moquegua and Tacna) and northern Chile (Sulca et al., 2018; Peng et al., 2019).

Peru has experienced devastating precipitation-related disasters associated with El Niño Costero in the past, most notably during the 2017 event, which caused widespread socioeconomic impacts across central Peru (Rodríguez-Morata et al., 2019). During the event, an increased frequency of cold air incursions from the subtropics interacted with the South American Low-Level Jet (SALLJ), enhancing moisture convergence over the eastern Andean foothills. This moisture was then transported upslope, sustaining long-duration precipitation systems over the central Andes (Chavez et al., 2020) contributing to widespread flooding in Andean valleys (Ramírez & Briones, 2017). This event resulted in 3.1 billion dollars of monetary loss, 138 deaths, 459 injuries, and affected 1.74 million people (French et al. 2020).

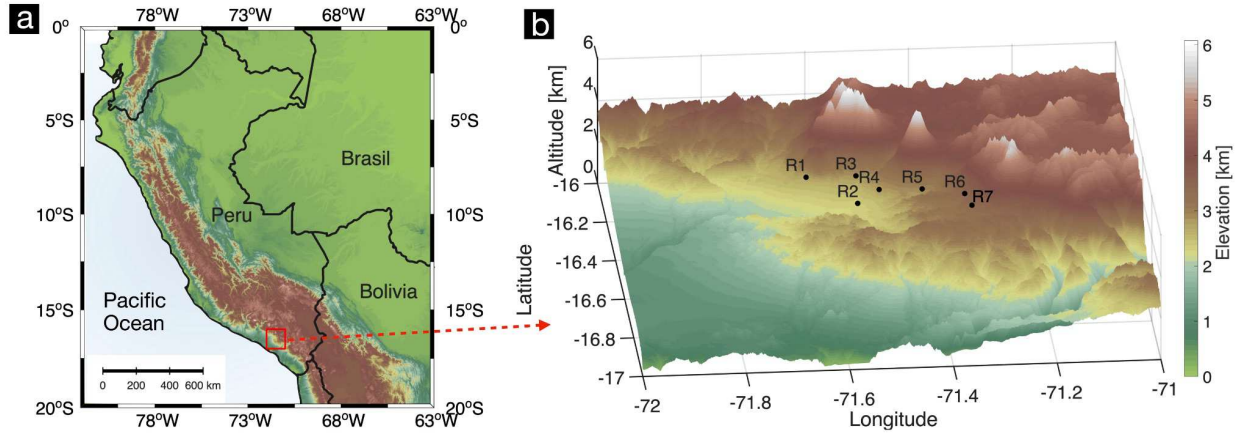

Fig. 1 (a) Map of Peru and the study region in the Tropical Andes of southern Peru as a red square. (b) Digital Elevation Model from the Advanced Land Observing Satellite (ALOS) of the study region (red square in panel a) centered on Arequipa city and the location of rain gauges are the black dots with short names (R1-R7).

In February 2026, rapid-onset Coastal El Niño conditions (ENFEN, 2026) contributed to above-average rainfall across the Tropical Andes of Southern Peru (TASP; Fig. 1), triggering two consecutive flash floods and mudslides within a three-day period in Arequipa, Peru's second-largest city. These recurrent, high-impact events associated with Coastal El Niño pose a major threat to communities and infrastructure across the region. Modeling these events and developing effective early warning systems remain challenging because of the limited availability of ground-based observations. Therefore, there is a critical need to better understand the atmospheric processes driving Coastal El Niño–triggered extreme precipitation events in southern Peru and to assess the capability of satellite-based precipitation products to capture their spatial and temporal evolution, with implications for precipitation monitoring and early warning in this data-sparse region.

In this study, we examine the atmospheric conditions associated with the two extreme precipitation events that affected Arequipa on 19 and 22 February 2026. Then, three widely used satellite precipitation products are evaluated in capturing the timing, magnitude, and spatial distribution of rainfall during the two events. This analysis provides insights into the meteorological processes underlying extreme precipitation in southern Peru and the ability of satellite observations to characterize such events in a region where ground-based observations are limited.

2. Datasets and Methods

2.1 Satellite-based Quantitative Precipitation Estimates

Near-real-time and standard versions of three widely used satellite-based precipitation products—IMERG, GSMaP, and PERSIANN—are used to investigate two consecutive flood events that occurred in February 2026 over Arequipa in southern Peru. The description of the precipitation products is highlighted in this section.

2.1.1 Integrated Multi-satellitE Retrievals for GPM (IMERG):

IMERG integrates passive microwave retrievals from the Global Precipitation Measurement constellation with infrared-based estimates using a morphing technique, followed by gauge calibration (Huffman et al. 2020). Three versions of IMERG quantitative precipitation estimates are available: Early, Late, and Final. IMERG-Early is the near-real-time product with a latency of ~4 hours, while IMERG-Late is a standard product available after ~14 hours. IMERG-Final is a research-grade product with a latency of 3–6 months. In this study, gauge-corrected quantitative precipitation estimates (QPEs) from Version 07 of the IMERG-Early and IMERG-Late products are used. Both datasets provide precipitation estimates at 0.1° spatial resolution and 30-minute temporal resolution. For consistency with other precipitation products, we convert half-hourly QPEs to hourly.

2.1.2 Global Satellite Mapping of Precipitation (GSMaP)

GSMaP, developed by the Japan Aerospace Exploration Agency, employs a Kalman filter-based approach to propagate microwave-derived precipitation using geostationary infrared observations (Kubota et al. 2026). Gauge-adjusted variants are also available. This study uses the near-real-time GSMaP-NRT and the standard GSMaP-MVK products. GSMaP-NRT has a latency of ~4 hours, whereas GSMaP-MVK has a latency of 3 days. Version 08 products with hourly temporal resolution and 0.1° spatial resolution are used in this study.

2.1.3 Precipitation Estimation from Remotely Sensed Information using Artificial Neural Networks (PERSIANN)

PERSIANN is developed by the Center for Hydrometeorology and Remote Sensing and uses artificial neural networks to relate infrared satellite observations to surface precipitation (Nguyen et al 2018). The near-real-time product used in this study is PDIR-Now, which has a latency of less than 1 hour and the standard PERSIANN product has a latency of 2 days. Both the datasets are available at hourly temporal resolution. The spatial resolution of PDIR-Now and PERSIANN is 4 km and 0.25°.

2.2 ERA-5 Model Reanalysis:

ERA5 (ECMWF Reanalysis v5; Hersbach et al., 2020) is the fifth-generation global atmospheric reanalysis produced by the European Centre for Medium-Range Weather Forecasts (ECMWF). ERA5 pressure-level reanalysis (Hersbach et al., 2023) at 0.25° horizontal resolution and hourly temporal resolution was used to obtain horizontal moisture flux from specific humidity (q) and horizontal winds (u,v). Total precipitation and surface winds were taken from the ERA5-Land reanalysis (Muñoz-Sabater et al., 2021), which runs the land component of ERA5 at an enhanced horizontal resolution of 0.1° (~9 km). The combination of ERA5 pressure-level data and ERA5-

Land allowed the characterization of both the vertical structure of moisture transport and the resulting surface precipitation patterns.

2.3 Rain Gauges

Hourly precipitation records from rain gauge stations across the Arequipa region of Peru were obtained from the Servicio Nacional de Meteorología e Hidrología del Perú (SENAMHI). A total of seven rain gauges are located within the study region, with their spatial distribution shown in Fig. 1b. The geographical coordinates and elevations of the seven rain gauge stations are provided in Table S1 of the Supplementary Information.

2.4 Evaluation Metrics

Statistical metrics are used to evaluate the detection and estimation performance of the satellite precipitation products. For precipitation detection, a threshold of 0.2 mm/h^{-1} is considered. The detection performance is evaluated using the Probability of Detection (POD), False Alarm Ratio (FAR), Critical Success Index (CSI), and Heidke Skill Score (HSS). The estimation performance is calculated using the Root Mean Square Error (RMSE) and Relative Bias (RB). The formulations of these evaluation metrics are provided in the Supplementary Information, Section S1.

3. February Floods in Arequipa

Arequipa (2300 m a.s.l.; 16.4°S, 71.4°W; Fig. 1b) is Peru's second largest city, located on the lower western and southwestern flanks of Misti (5822 m a.s.l.) and Chachani (6057 m a.s.l.) volcanoes. Flash floods and debris flows represent a significant hazard to Arequipa, where populations living near ravines (locally called quebradas or torrenteras) are particularly vulnerable because of their exposure to flood- and debris-flow-prone areas (Thouret et al., 2013). On 19 and 22 February 2026, Arequipa experienced two flash-flood events three days apart, causing fatalities, infrastructure damage, and widespread disruption affecting thousands of people. On 19 February 2026, a thunderstorm with heavy rainfall and hail triggered debris flows along Quebrada Chullo. A second rainfall event on 22 February produced additional debris flows and flooding (INDECI, 2026; Fig. 2). These events, which occurred under El Niño Costero conditions, resulted in 6 direct and 15 indirect fatalities, affected 5,596 people, damaged 1,706 homes, and impacted 4 educational institutions, 5 health facilities, and 51 hectares of agricultural land (INDECI, 2026). The post-event geological assessment from the Instituto Geológico Minero y Metalúrgico - Dirección de Geología Ambiental y Riesgo Geológico (2026) found that intense rainfall of about 20–35 $mm\ h^{-1}$ in the upper part of Quebrada Chullo, together with the strongly reduced width of the channelized urban reach of Quebrada Chullo, produced debris-flow overflow and flooding along the ravine, particularly in the constricted urban sections of Cayma, Yanahuara, and Cercado de Arequipa.



Fig. 2 Impacts of flooding, mudslides and debris flow after the two intense convective episodes in Arequipa, Peru captured on (a) Febraury 22, 2026 and (b) Febraury 23, 2026. Photograph by Froylan Quirita.

Although the Arequipa region lacks weather radar coverage, seven SENAMHI rain gauges are distributed along the western slopes of the Andes surrounding the city (Fig 1.b). On February 19, at 15:00 LT the rain gauge in Cayma district (at 2800 m a.s.l; R3 in Fig 1.b) just above Arequipa City measured 20.8 mm within 1 hour associated with an afternoon thunderstorm accompanied by heavy rainfall and hail. On 22 February, a second extreme rainfall of 34.1 mm within 1 hour in Cayma generated a further flood. The 6-hour rainfall totals (Fig. 3) from the seven gauges during the same period reveal a strong spatiotemporal variation in precipitation. The most western rain gauges (R1, R3, R4 and R7) received higher rainfall during 19 February, contributing to the first flood event, while the eastern gauges (R3, R5 and R6) recorded higher precipitation on 22 February, associated with the second flood event. Moreover, most rainfall episodes during this week occurred during the afternoon hours and short-lived.

The mechanisms behind this short duration intense convective precipitation events are investigated using surface winds from ERA5-Land. Accumulated precipitation and mean surface winds from ERA5-Land during 19-22 February, 2026 (Fig. 4a), when superimposed on a digital elevation

model (Fig. 4b), reveal that the heaviest rainfall occurred on the windward slopes. This spatial pattern strongly supports the hypothesis that these short duration intense convective precipitation events were triggered by Pacific air flow mechanically forced by the Arequipa Volcanoes (Fig 4b). ERA5-Land precipitation accumulation during 19-22 February shows an intense rainfall maximum over Arequipa City and the surrounding districts agreeing closely with most of the SENAMHI rain gauges (circles in Fig 3a,b). Three gauges (R2, R4 and R7) out of the total seven SENAMHI rain gauges recorded comparatively lower total precipitation accumulation and demonstrated a spatial gradient.

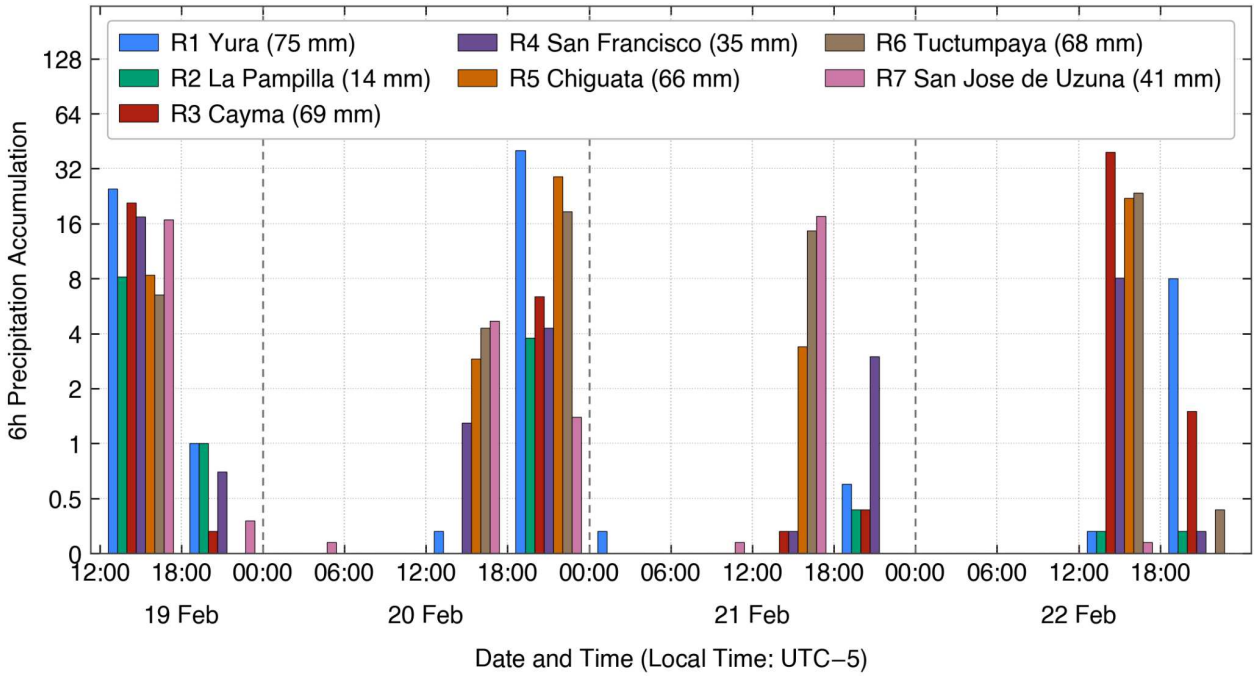

Fig. 3 Time series of six-hourly precipitation accumulation from the rain gauges.

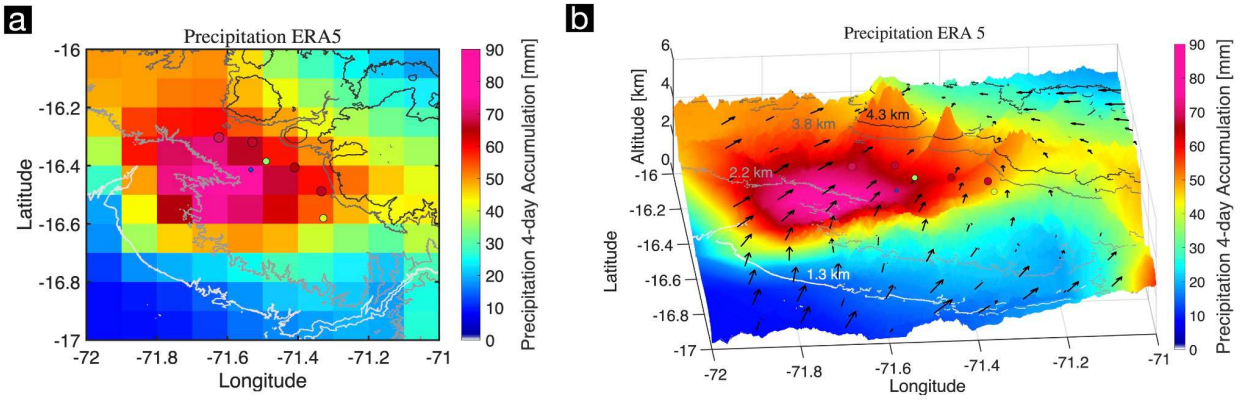

Fig. 4 (a) ERA5-Land total precipitation (shading) and raingauge (filled circles) accumulated precipitation in mm during 19–22 February 2026. White, light gray, dark gray, and black contour lines indicate elevations of 1.3, 2.2,

3.8, and 4.3 km, respectively. (b) Same as (a) but superimposed on the ALOS digital surface model with mean surface winds positioned for visualization at 300m above the ground.

4. Results

4.1 Atmospheric Drivers Contributing to the Flood Events

Horizontal moisture fluxes and wind fields from ERA5 reanalysis are used to characterize the meteorological conditions that contributed to the two intense precipitation events that occurred in February 2026 in Arequipa. Mean horizontal moisture fluxes and wind fields (Fig. 5) reveal that moisture reached the TASP from two distinct sources: Amazonian air at 550 hPa and Pacific air at 850 hPa. Along the eastern Andean foothills between 10°S and 15°S, the typical South American Low-Level Jet (SALLJ) moisture pattern was suppressed by a cold-air incursion flowing opposite to the climatological SALLJ (Fig. 5a-c). However, south of 16°S, the SALLJ re-emerged. A zonal cross-section (Fig. 5d) at 16.5°S (along Arequipa City) shows low-level easterly moisture fluxes from the Pacific impinging directly on the western slopes of the Andes near 2 km altitude. Above 4 km, Amazonian moisture crossed the Andes from east to west, consistent with typical wet-season conditions. However, this Amazonian moisture transport was slightly reduced on 19 February and strongly reduced on 22 February during the respective afternoon thunderstorm events (Figs. 5e,f). In contrast, low-level moisture originating from the Pacific substantially increased moisture availability over the western slopes of the Andes on both days, with the Pacific moisture penetrating significantly farther eastward on 22 February than on 19 February.

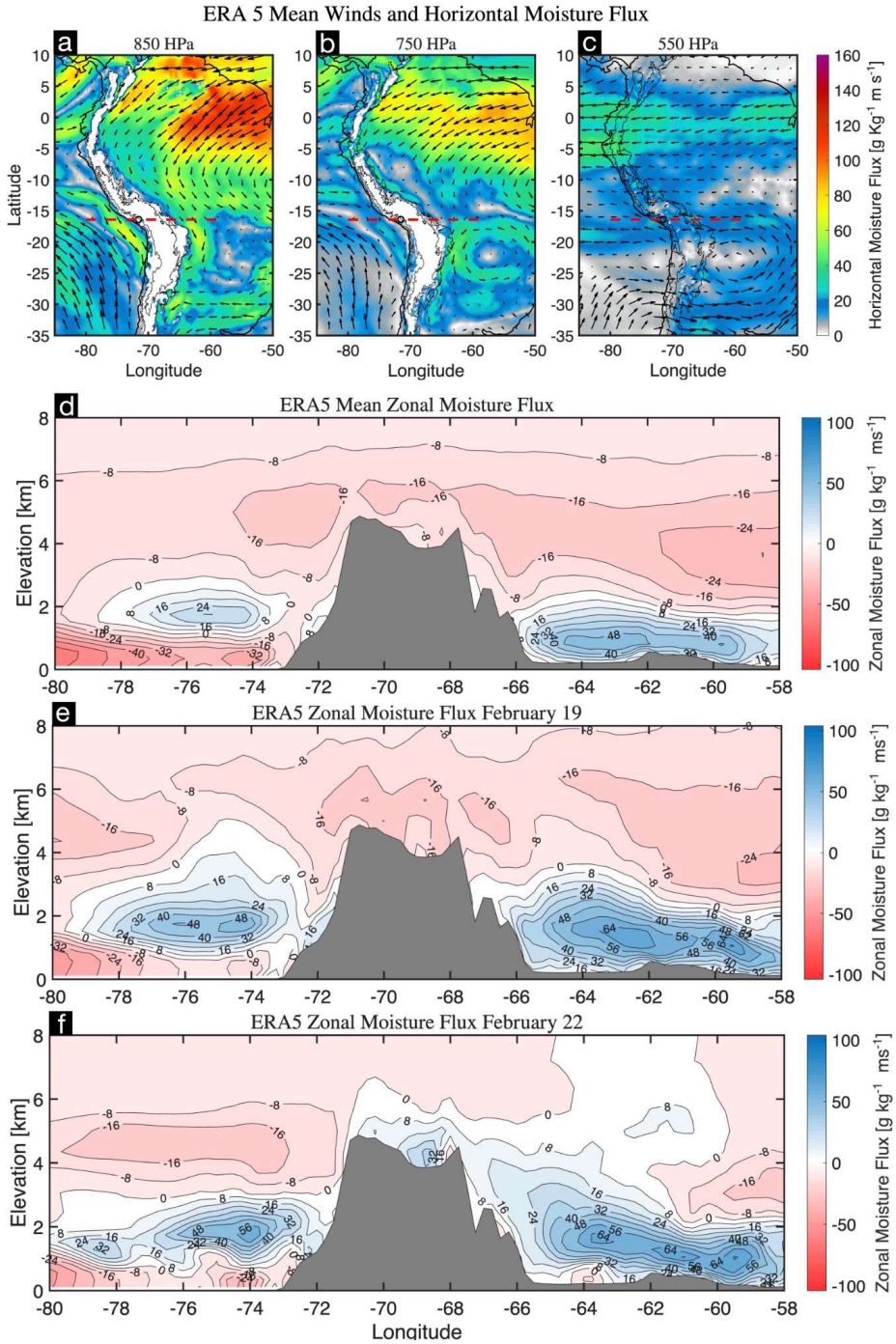

Fig 5. Mean atmospheric moisture transport over the Tropical Andes during 19–22 February 2026. (a–c) Mean horizontal wind vectors and moisture fluxes (shading) at (a) 850 hPa, (b) 750 hPa, and (c) 550 hPa. (d) Vertical cross-section of zonal moisture flux (kg m^{-1} s^{-1}) along 16.5°S (red dashed line in a–c), crossing the city of Arequipa (black circle in a–c). (e) Vertical cross-section of zonal moisture flux (kg m^{-1} s^{-1}) along 16.5°S (red dashed line in a–

c), crossing the city of Arequipa (black circle in a–c) on February 19 between 13-19 hours local time. (f) Same as (e) but for February 22. The Andes are depicted as a gray area in all cross sections.

4.2 Performance of Satellite Precipitation Products

4.2.1 Four-day Total Precipitation Accumulation:

Figure 6 shows the 4-day accumulated precipitation over the study region shown in Fig. 1.b. Despite differences in spatial resolution, the three satellite precipitation products—GSMaP, PERSIANN, and IMERG—exhibit distinct spatial patterns. The GSMaP (Fig. 6a and d) products show a relatively uniform distribution of precipitation across the study region, whereas PERSIANN (Fig. 6b and e) indicates higher precipitation toward the center of the region. In contrast, IMERG (Fig. 6c and f) shows enhanced precipitation along the 3–4 km elevation contours, suggesting a stronger association with the regional topography. The rain gauges are distributed primarily along these 3–4 km elevation contours and capture substantial spatial heterogeneity in precipitation. In particular, the easternmost gauge, R1 (Yura), records a maximum 4-day accumulation of 75.2 mm, while R2 (La Pampilla) records only 13.8 mm over the same period.

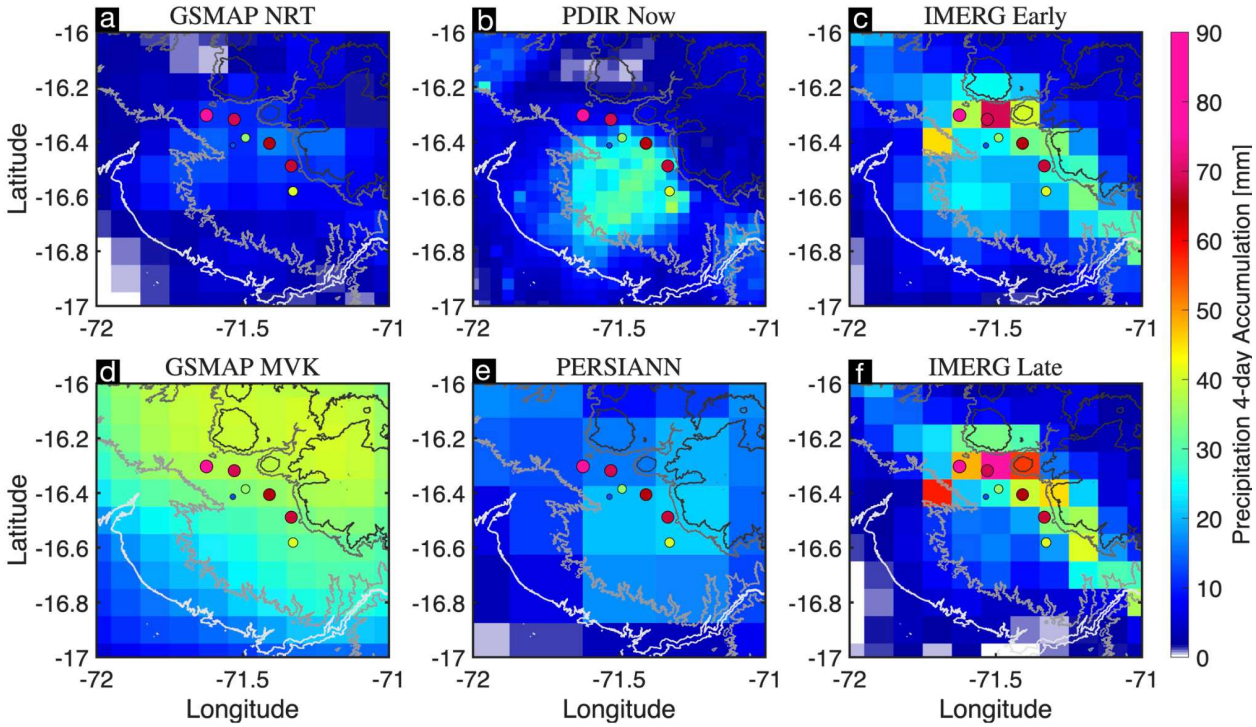

Fig 6. Total precipitation accumulated during 19–22 February 2026 over southern Peru from three near-real-time satellite precipitation products (a-c) and their Late-corrected versions (d-f). Circle markers indicate 4-day accumulated precipitation measured by rain gauges; marker size is proportional to precipitation amount and marker

fill color follows the scale bar. White, light gray, dark gray, and black contour lines show terrain elevations of 1.3, 2.2, 3.8, and 4.3 km, respectively.

The 4-day precipitation accumulation from the rain gauges and the corresponding nearest satellite precipitation pixels, along with their percentage biases, are presented in Table 1. Overall, the standard, late-corrected products (Figs. 6d–f) show improved performance in capturing precipitation intensity compared with their near-real-time counterparts. In particular, IMERG-Late (Fig. 6f) retains the spatial structure observed in IMERG-Early (Fig. 6c) while estimating comparatively higher precipitation amounts. Consequently, IMERG-Late provides the best estimate of 4-day precipitation accumulation for four of the seven gauges. GSMaP-MVK (Fig. 6d) and PERSIANN (Fig. 6e) similarly show higher maximum precipitation and total accumulation compared with their respective near-real-time versions. Among the individual gauges, PERSIANN provides the closest estimate at R2, while GSMaP-MVK and IMERG-Early produce the best estimates at R4 and R3, respectively.

Table 1: Comparison of four-day precipitation accumulation (19–22 February 2026) between rain-gauge observations and satellite precipitation products, with corresponding percentage biases. Bold values indicate the best performing satellite product

Rain Gauges [Total Precipitation Accumulation in mm]	Total Precipitation Accumulation in mm [Bias in %]					
	GSMaP NRT	GSMaP MVK	PDIR-Now	PERSIANN	IMERG Early	IMERG Late
R1 - Yura [75.2]	11.5 [-84.7]	36.6 [-51.4]	5.6 [-92.5]	16.1 [-78.6]	37.9 [-49.6]	**48.2 [-36.0]**
R2 - La Pampilla [13.8]	10.9 [-21.1]	34.0 [146.1]	20.9 [51.2]	**16.1 [16.5]**	23.9 [73.3]	26.2 [89.6]
R3 - Cayma [68.9]	9.4 [-86.4]	36.0 [-47.7]	4.3 [-93.8]	15.0 [-78.3]	**59.5 [-13.6]**	86.1 [25.0]
R4 - San Francisco [35.2]	11.5 [-67.4]	**37.2 [5.6]**	21.5 [-38.9]	19.2 [-45.6]	38.3 [8.8]	54.1 [53.8]
R5 - Chiguata [65.7]	16.3 [-75.1]	33.6 [-48.9]	20.6 [-68.6]	20.0 [-69.5]	31.2 [-52.5]	**38.7 [-41.1]**
R6 - Tuctumpaya [68.0]	14.4 [-78.8]	35.5 [-47.9]	22.0 [-67.7]	19.2 [-71.8]	33.3 [-51.1]	**44.7 [-34.2]**
R7 - San Jose de Uzuna [41.2]	10.6 [-74.2]	32.7 [-20.5]	22.8 [-44.7]	21.8 [-47.2]	26.7 [-35.2]	**33.8 [-18.1]**

4.2.2 Temporal Evolution of Hourly Precipitation

Figure 7 shows the hourly evolution of precipitation recorded at the seven SENAMHI rain gauges (R1–R7) and compares the observations with six satellite precipitation products during 19–22

February 2026. Distinct afternoon rainfall bursts, with peak intensities exceeding 20 mm h^{-1}, were observed particularly on 19, 20, and 22 February 2026. These intense, short-duration events highlight the strong diurnal nature of precipitation during the study period.

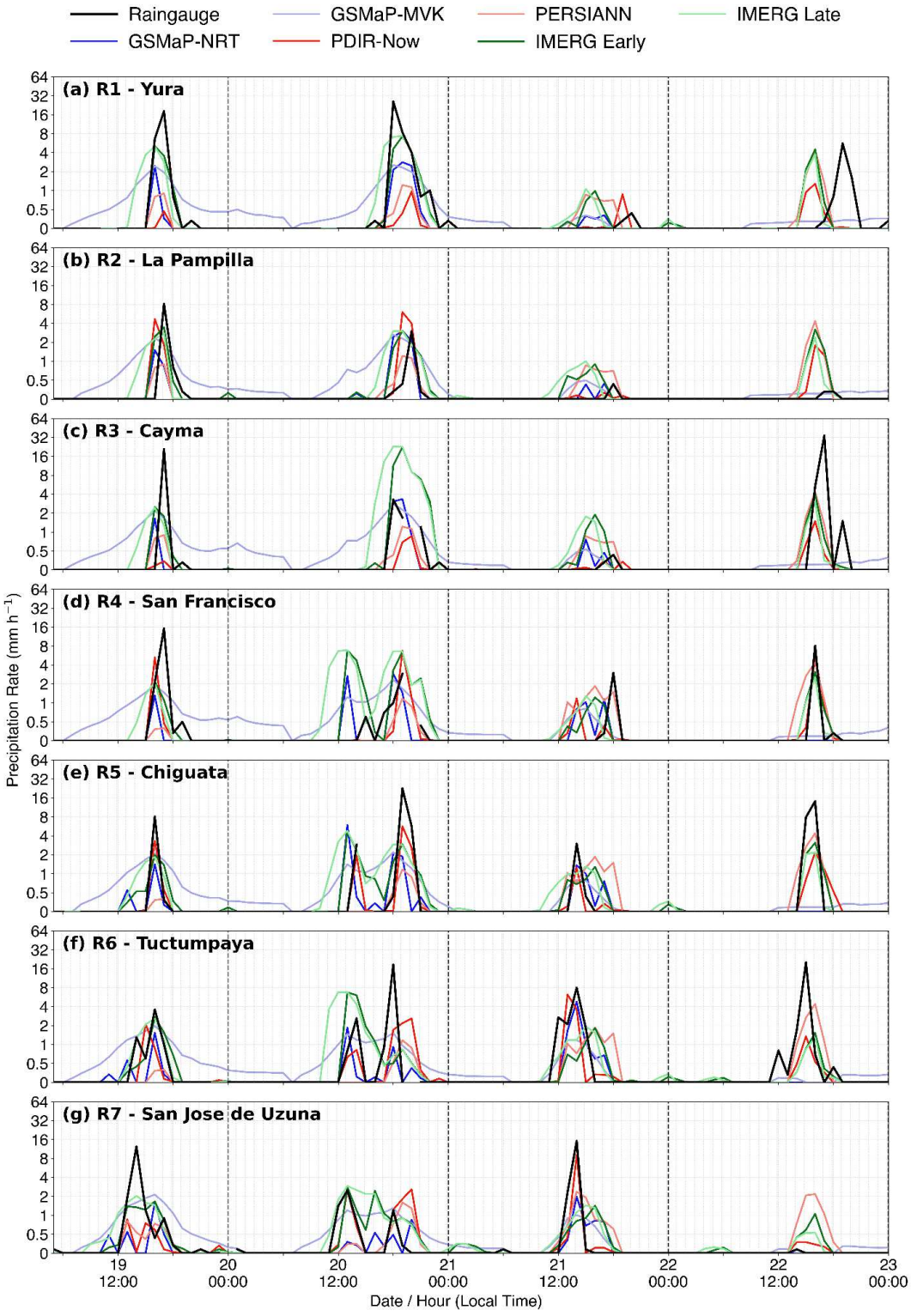

Fig 7. Time series of hourly precipitation rates from 19–22 February 2026 for seven rain gauges located in the Arequipa region, compared with the nearest satellite-based precipitation estimates from the near-real-time and standard versions of GSMaP, PERSIANN and IMERG.

On 19 February, gauges R1, R3, R4, and R7 recorded hourly precipitation rates of at least 16 mm/h, while R1, R5, and R6 recorded hourly precipitation rates of approximately 16 mm/h on 20 February 2026. All satellite precipitation products underestimated these observed peak intensities, whereas precipitation at locations with comparatively lower intensities was generally better represented by the satellite products. Overall, the satellite products captured the timing of the precipitation events reasonably well. However, IMERG-Late detected the onset of the afternoon showers approximately 2 h earlier than IMERG-Early. GSMaP-MVK produced spurious light precipitation throughout 19 and 20 February, across all the gauges (Fig 7).

During the second flood event on 22 February 2026, R3 (Cayma) recorded the highest hourly precipitation rate, reaching approximately 32 mm/h (Fig. 7c). At R1, the IMERG and PERSIANN products detected the peak approximately 3 h earlier than observed. These products also overestimated the precipitation rates at R2 and R7. While the satellite products generally captured the timing of the precipitation events, they also tended to underestimate the intensity of the extreme precipitation events.

The overall detection and estimation performance at the hourly scale is summarized in Table 2. In terms of detection performance, GSMaP-MVK achieves the highest Probability of Detection (POD; 0.761), followed by IMERG-Early (0.739) and IMERG-Late (0.738), indicating that these products were more successful in detecting precipitation event. However, GSMaP-MVK also exhibits the highest False Alarm Ratio (FAR; 0.765), consistent with the spurious light precipitation detected throughout 19 and 20 February. PDIR-Now has the lowest FAR (0.333), but its relatively low POD (0.543) indicates that it also missed a considerable number of observed precipitation events. IMERG-Early achieves the highest Critical Success Index (CSI; 0.430), indicating the best balance between correct detections, missed events, and false alarms. PDIR-Now has the highest Heidke Skill Score (HSS; 0.541), suggesting the strongest overall detection skill among the evaluated satellite products.

For precipitation estimation, the PERSIANN products exhibit the lowest RMSE values, indicating the smallest magnitude of errors relative to the rain gauge observations. Although these products generally underestimated the precipitation intensity during the first two events, their lower RMSE suggests comparatively better agreement with the observed hourly precipitation rates across the full evaluation period. In terms of relative bias, IMERG-Late exhibits the smallest overall bias, indicating the closest agreement with the observed accumulated precipitation. These results

highlight that the product with the best categorical detection performance does not necessarily exhibit the best quantitative estimation performance

Table 2: Detection and precipitation estimation performance of the satellite precipitation products against rain-gauge observations. Detection metrics are calculated using a precipitation threshold of 0.2 mm h^{-1}. Bold values indicate the best performance for each metric.

Satellite Products	Detection Metrics [0.2 mm/h threshold]				Estimation Metrics	
	POD	FAR	CSI	HSS	RMSE	Bias (%)
GSMaP-NRT	0.413	0.415	0.319	0.417	2.742	-77.01
GSMaP-MVK	**0.761**	0.765	0.219	0.185	2.689	-33.30
PDIR-Now	0.543	**0.333**	0.427	**0.541**	**2.627**	-68.03
PERSIANN	0.652	0.492	0.400	0.492	2.681	-65.43
IMERG-Early	0.739	0.493	**0.430**	0.523	2.751	-31.86
IMERG-Late	0.738	0.579	0.364	0.434	2.935	**-9.84**

5 Conclusions

The two major flood-producing precipitation events in Arequipa, Peru, on 19 and 22 February 2026 highlight the challenges of monitoring short-duration, intense rainfall in the complex topography of the Tropical Andes. Enhanced low-level Pacific moisture transport during El Niño Costero interacting with the steep western slopes of the Andes caused these localized afternoon convection and intense rainfall.

To assess the ability of existing satellite precipitation products to capture this event, six satellite precipitation products with different latencies were evaluated against observations from seven SENAMHI rain gauges. The results demonstrate substantial differences among the products and across the detection and estimation metrics. GSMaP-MVK achieved the highest Probability of Detection (POD), but also exhibited a high False Alarm Ratio (FAR) associated with persistent spurious light precipitation. IMERG-Early achieved the highest Critical Success Index (CSI), while PDIR-Now had the highest Heidke Skill Score (HSS). IMERG-Late provided the closest representation of the overall precipitation accumulation; however, it detected the rainfall onset approximately 2–3 h earlier than raingauges and IMERG-Early. Overall, the results from this event suggest that the near-real-time versions of the evaluated products generally provided more

consistent representations of the observed precipitation than their corresponding late or standard versions.

The present analysis focuses on a single impactful flood episode and demonstrates the value of event-based evaluation for identifying product-specific strengths and limitations that may not be evident from bulk statistics alone. A systematic extension of this analysis to a larger set of impactful precipitation and flood events is needed to determine the consistency of these performance characteristics. Moreover, the varied strengths and limitations identified across the satellite products motivate the development of a merged satellite precipitation framework that can leverage their complementary characteristics. Such a framework could potentially reduce false alarms, improve the representation of intense precipitation, and better constrain the timing and spatial distribution of rainfall. This type of region-specific satellite precipitation product could be particularly valuable in the Tropical Andes, where weather radar coverage is limited and rain gauge networks are often too sparse to adequately characterize highly localized precipitation. Improving satellite-based precipitation estimates through multi-product merging could therefore provide an important foundation for developing more reliable flood monitoring and early warning systems in data-sparse regions.

6 Acknowledgments

The authors acknowledge the Servicio Nacional de Meteorología e Hidrología del Perú (SENAMHI) for providing rain gauge data of Arequipa.

7 Conflict of Interest Disclosure

The authors declare there are no conflicts of interest for this manuscript.

8 References

Cai, W., McPhaden, M. J., Grimm, A. M., Rodrigues, R. R., Taschetto, A. S., Garreaud, R. D., Dewitte, B., Poveda, G., Ham, Y.-G., Santoso, A., Ng, B., Anderson, W., Wang, G., Geng, T., Jo, H.-S., Marengo, J. A., Alves, L. M., Osman, M., Li, S., … Vera, C. (2020). Climate impacts of the El Niño–Southern Oscillation on South America. Nature Reviews Earth & Environment, 1(4), 215–231. https://doi.org/10.1038/s43017-020-0040-3

Castellares, R., García, M. F., & Vicuña, J. (2025). Natural events in Peru: A multidimensional analysis. Banco Central de Reserva del Perú.

Chavez, S. P., Silva, Y., & Barros, A. P. (2020). High-Elevation Monsoon Precipitation Processes in the Central Andes of Peru. Journal of Geophysical Research: Atmospheres, 125(24), e2020JD032947. https://doi.org/10.1029/2020JD032947

Echevin, V., Colas, F., Espinoza-Morriberon, D., Vasquez, L., Anculle, T., & Gutierrez, D. (2018). Forcings and Evolution of the 2017 Coastal El Niño Off Northern Peru and Ecuador. Frontiers in Marine Science, 5, 367. https://doi.org/10.3389/fmars.2018.00367

ENFEN. (2026). Comunicado Oficial ENFEN. Retrieved May 27, 2026, from https://enfen.imarpe.gob.pe/download/comunicado-oficial-enfen-n-04-2026/

French, A., Mechler, R., Arestegui, M., MacClune, K., & Cisneros, A. (2020). Root causes of recurrent catastrophe: The political ecology of El Niño-related disasters in Peru. International Journal of Disaster Risk Reduction, 47, 101539. https://doi.org/10.1016/j.ijdrr.2020.101539

Hersbach H, Bell B, Berrisford P, et al. (2020). The ERA5 global reanalysis. Q J R Meteorol Soc., 146:1999–2049. https://doi.org/10.1002/qj.3803

Hersbach, H., Bell, B., Berrisford, P., Biavati, G., Horányi, A., Muñoz Sabater, J., Nicolas, J., Peubey, C., Radu, R., Rozum, I., Schepers, D., Simmons, A., Soci, C., Dee, D., Thépaut, J-N. (2023): ERA5 hourly data on pressure levels from 1940 to present. Copernicus Climate Change Service (C3S) Climate Data Store (CDS), DOI: 10.24381/cds.bd0915c6 (Accessed on 04-04-2026).

Huffman, G.J. et al. (2020). Integrated Multi-satellite Retrievals for the Global Precipitation Measurement (GPM) Mission (IMERG). In: Levizzani, V., Kidd, C., Kirschbaum, D.B., Kummerow, C.D., Nakamura, K., Turk, F.J. (eds) Satellite Precipitation Measurement. Advances in Global Change Research, vol 67. Springer, Cham. https://doi.org/10.1007/978-3-030-24568-9_19.

INDECI. (2026). Reporte Complementario N.º 2799. Retrieved August 16, 2026, from https://portal.indeci.gob.pe/wp-content/uploads/2026/02/REPORTE-COMPLEMENTARIO-

N.%C2%BA-2799-1MAR2026-LLUVIAS-INTENSAS-EN-LA-PROVINCIA-DE-AREQUIPA-AREQUIPA-19.pdf

Instituto Geológico Minero y Metalúrgico. Dirección de Geología Ambiental y Riesgo Geológico (2026). Evaluación geológica de las zonas afectadas por lluvias en Arequipa Metropolitana - febrero – 2026. Distritos Cayma, Yanahuara, Cerro Colorado, José Luis Bustamante y Rivero, Miraflores, Mariano Melgar y Paucarpata, Alto Selva Alegre y Arequipa (Cercado). INGEMMET, Informe Técnico N° A7737, 57P. Retrieved from https://repositorio.ingemmet.gob.pe/handle/20.500.12544/5380?locale=es

Kubota, T. et al. (2026). Construction of a Longer Term and more Homogeneous GSMaP Precipitation Dataset. In: Chandrasekar, V., Das, S., Datta, A. (eds) Radar Meteorology and its Applications. Springer Atmospheric Sciences. Springer, Singapore. https://doi.org/10.1007/978-981-95-5409-6_9

Lavado-Casimiro, W. S., Felipe, O., Silvestre, E., & Bourrel, L. (2013). ENSO impact on hydrology in Peru. Advances in Geosciences, 33, 33–39. https://doi.org/10.5194/adgeo-33-33-2013

Martinez-Villalobos, C., Dewitte, B., Garreaud, R. D., & Loyola, L. (2024). Extreme coastal El Niño events are tightly linked to the development of the Pacific Meridional Modes. Npj Climate and Atmospheric Science, 7(1), 123. https://doi.org/10.1038/s41612-024-00675-5

Muñoz-Sabater, J., Dutra, E., Agustí-Panareda, A., Albergel, C., Arduini, G., Balsamo, G., Boussetta, S., Choulga, M., Harrigan, S., Hersbach, H., Martens, B., Miralles, D. G., Piles, M., Rodríguez-Fernández, N. J., Zsoter, E., Buontempo, C., and Thépaut, J.-N. (2021). ERA5-Land: a state-of-the-art global reanalysis dataset for land applications, Earth Syst. Sci. Data, 13, 4349–4383. https://doi.org/10.5194/essd-13-4349-2021.

Nguyen, P., Ombadi, M., Sorooshian, S., Hsu, K., AghaKouchak, A., Braithwaite, D., Ashouri, H., and Thorstensen, A. R. (2018). The PERSIANN family of global satellite precipitation data: a review and evaluation of products, Hydrol. Earth Syst. Sci., 22, 5801–5816. https://doi.org/10.5194/hess-22-5801-2018.

Oswald Charca. (2026, Febraury 24). Cars are stuck in an inundated street after heavy rains flooded the neighbourhood with mud and debris, in Arequipa, Peru February 19, 2026. Reuters. https://www.reutersconnect.com/item/heavy-rains-cause-floods-and-infrastructure-damage-in-arequipa/dGFnOnJldXRlcnMuY29tLDIwMjY6bmV3c21sX1JDMkJQSkE3VE5FMw

Oswald Charca. (2026, Febraury 24). A drone view of apartment buildings and streets filled with muddy water following a flash flood caused by torrential rains, in Arequipa, Peru, February 23, 2026. Reuters. https://www.reutersconnect.com/item/flash-flood-caused-by-torrential-rains-in-arequipa/dGFnOnJldXRlcnMuY29tLDIwMjY6bmV3c21sX1JDMlFSSkFDOEtHRw

Peng, Q., Xie, S.-P., Wang, D., Zheng, X.-T., & Zhang, H. (2019). Coupled ocean-atmosphere dynamics of the 2017 extreme coastal El Niño. Nature Communications, 10(1), 298. https://doi.org/10.1038/s41467-018-08258-8

Ramírez, I. J., & Briones, F. (2017). Understanding the El Niño Costero of 2017: The Definition Problem and Challenges of Climate Forecasting and Disaster Responses. International Journal of Disaster Risk Science, 8(4), 489–492. https://doi.org/10.1007/s13753-017-0151-8

Rodriguez-Morata, C., Díaz, H. F., Ballesteros-Canovas, J. A., Rohrer, M., & Stoffel, M. (2019). The anomalous 2017 coastal El Niño event in Peru. Climate Dynamics, 52(9), 5605-5622

Sulca, J., Takahashi, K., Espinoza, J., Vuille, M., & Lavado-Casimiro, W. (2018). Impacts of different ENSO flavors and tropical Pacific convection variability (ITCZ , SPCZ) on austral summer rainfall in South America, with a focus on Peru. International Journal of Climatology, 38(1), 420–435. https://doi.org/10.1002/joc.5185

Thouret, J.-C., Enjolras, G., Martelli, K., Santoni, O., Luque, J. A., Nagata, M., Arguedas, A., and Macedo, L.: Combining criteria for delineating lahar- and flash-flood-prone hazard and risk zones for the city of Arequipa, Peru, Nat. Hazards Earth Syst. Sci., 13, 339–360, https://doi.org/10.5194/nhess-13-339-2013, 2013.

Young, K. R., & León, B. (2009). Natural hazards in Peru: causation and vulnerability. Developments in earth surface processes, 13, 165-180. https://doi.org/10.1016/S0928-2025(08)10009-8

Supplementary Files

This is a list of supplementary files associated with this preprint. Click to download.

- SupplementaryInformation.pdf